Available online at www.sciencedirect.com

SCIENCE DIRECT®

Journal of Sound and Vibration 288 (2005) 1131–1155

JOURNAL OF SOUND AND VIBRATION

www.elsevier.com/locate/jsvi

Nonlinear control of a shape memory alloy adaptive tuned vibration absorber

Keith A. Williams[a,*], George T.-C. Chiu[b], Robert J. Bernhard[b]

[a]Department of Mechanical Engineering, The University of Alabama, 164 Hardaway Hall, P.O. Box 870276, Tuscaloosa, AL 35487-0276, USA
[b]1077 Herrick Laboratories, Purdue University, West Lafayette, IN 47907-1077, USA

Received 8 September 2004; received in revised form 5 January 2005; accepted 25 January 2005
Available online 13 June 2005

Abstract

The adaptive-passive approach to vibration control shows potential for achieving superior performance when compared to classical passive solutions. On-line adaptation of passive elements is central to the adaptive-passive approach and a great deal of research has focused on determining methods to realize the physical adaptation of the vibration control system. However, very little effort has been put into designing feedback laws to close the loop and control on-line adaptation to achieve desired performance. This paper discusses the design and analysis of a controller to tune an adaptive-passive vibration control system, in this case a shape memory alloy (SMA) adaptive-tuned vibration absorber (ATVA). Tuning of the SMA ATVA is achieved through appropriate heating and cooling of SMA beam elements. The SMA ATVA controller is designed using a model developed in a previous study. A Lyapunov analysis is presented to demonstrate stability of the system under proportional–integral (PI) control when saturation of the control effort is neglected. However, severe control saturations can occur in response to excitation profiles that call for rapid cooling of the SMA beam elements. Without active cooling, integrator windup results, particularly if high gains are used. To deal with the windup, a nonlinear PI controller with integrator reset was developed. A second Lyapunov analysis is used to demonstrate stability of the modified system. Experimental results are included that demonstrate the improved performance of the system with the nonlinear controller.

---

[*] Corresponding author. Tel.: +1 205 348 2605; fax: +1 205 348 6419.
E-mail address: kwilliams@coe.eng.ua.edu (K.A. Williams).

0022-460X/$ - see front matter © 2005 Elsevier Ltd. All rights reserved.
doi:10.1016/j.jsv.2005.01.018

1. Introduction

Adaptive-passive vibration control involves on-line adaptation of passive elements of the vibration control system to realize vibration control. The most common adaptive-passive device is the adaptive tuned vibration absorber (ATVA), a mass–spring–damper assembly mounted to a primary system exposed to harmonic excitation. Like a classical tuned vibration absorber (TVA), a lightly damped ATVA will provide significant attenuation of the primary system's vibration when the excitation frequency ω_{exc} matches the absorber natural frequency ω_{abs}. In an ATVA, ω_{abs} is tuned to track an uncertain or drifting ω_{exc}, resulting in improved performance when compared to that achieved with a standard TVA. The improvement is particularly noticeable when ω_{exc} drifts and coincides with a resonant frequency of the primary system. With a passive TVA, such an event is a distinct possibility as implementation of a TVA introduces a new resonant peak in the primary system's frequency response that, in some cases, is quite close to ω_{abs}.

A number of methods are available for realizing ATVA designs and are described in the works by Sun et al. [1] and Williams et al. [2]. Methods include moving an end mass on a beam as described by Seto and Tominari [3], the variable-length coil spring of Franchek et al. [4], the variable leaf-spring design of Walsh and Lamancusa [5], the shunted piezoelectric patch of Hollkamp and Starchville [6], the piezoceramic inertial actuator (PIA) of Davis and Lesieutre [7], the magnetostrictive absorber described by Flatau et al. [8], and the shape memory alloy (SMA) ATVA developed by Williams et al. [9].

Different control paradigms have been used to tune an ATVA in real time. Seto and Tominari [3] and Walsh and Lamancusa [5] utilized open-loop approaches to match ω_{abs} to ω_{exc}. The open-loop approaches have the advantage of simplicity, but may not be robust. Robust performance requires closed-loop control that can accommodate changes or uncertainties in the ATVA design and response. Hollkamp and Starchville [6] used a closed-loop gradient-search technique that sought to minimize the primary system response. Davis and Lesieutre [7] monitored ω_{exc} and used that information to determine the appropriate capacitive shunt to modify ω_{abs} of their PIA.

Franchek et al. [4] and Buhr et al. [10] framed the problem in a classical feedback control framework by examining the response of a system with an undamped TVA applied. For that case, the optimum condition is indicated by the relative phase between the vibration of the absorber and the excitation input, ϕ_{rel}. At the optimum condition, $\omega_{\text{abs}} = \omega_{\text{exc}}$, $\phi_{\text{rel}} = -90^\circ$, and thus $\cos(\phi_{\text{rel}}) = 0$. For the case of $\omega_{\text{abs}} < \omega_{\text{exc}}$, $\cos(\phi_{\text{rel}}) < 0$ and for $\omega_{\text{abs}} > \omega_{\text{exc}}$, $\cos(\phi_{\text{rel}}) > 0$, such that the sign of $\cos(\phi_{\text{rel}})$ can be used to determine the appropriate tuning direction. That approach was successfully demonstrated although no formal stability analysis was performed. It is important to note that in the presence of damping, the exact optimal condition is no longer indicated by $\cos(\phi_{\text{rel}}) = 0$. However, Williams et al. [2] demonstrated that, for lightly damped ATVA systems, using $\cos(\phi_{\text{rel}}) = 0$ as an indicator of the optimal condition will not result in significant performance loss.

Thus, $\cos(\phi_{\text{rel}})$ is a reasonable indicator of an ATVA's tuned condition and a logical error signal for a controller acting to tune the ATVA. A sketch of the behavior of $\cos(\phi_{\text{rel}})$ as a function of the relative frequencies ω_{abs} and ω_{exc} is shown in Fig. 1. $\cos(\phi_{\text{rel}})$ is a nonlinear function of ω_{abs} and ω_{exc}. For large mismatches between ω_{abs} and ω_{exc}, ϕ_{rel} approaches either 0 or π, $\cos(\phi_{\text{rel}}) \approx \pm 1$, and the gain is small. However, the gain increases for ω_{abs} approaching ω_{exc} and may be quite

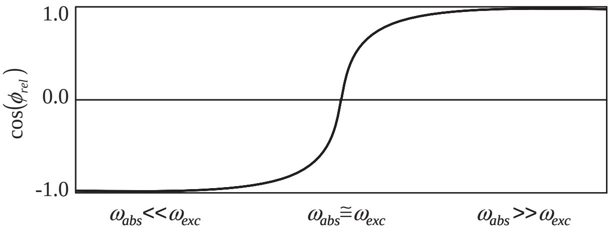

Fig. 1. Variation of ϕ_{rel} with relative locations of ω_{abs} and ω_{exc}.

large for $\omega_{\text{abs}} \approx \omega_{\text{exc}}$. This type of behavior creates certain difficulties for controller design. Large controller gains will be necessary to achieve performance in the low-gain regions, but those same gains will lead to excessive overshoot and integrator windup in the high-gain region near $\omega_{\text{abs}} \approx \omega_{\text{exc}}$. Saturation in control effort will further complicate the controller design, as it will contribute to the problem of integrator windup. Such saturation is anticipated in a system using thermal actuation, particularly when active cooling is not implemented.

In this paper the development of a feedback controller designed to deal with the specific nonlinearities inherent in an SMA ATVA is described. The paper builds on the earlier work of Williams et al. [2], where the development and modeling of an SMA ATVA were described. A proportional–integral (PI) control law is developed and shown to be stable in the absence of control signal saturation. Saturation is an issue, however, and when included in the analysis, the system is no longer guaranteed stable. A phase-plane analysis is used to develop certain modifications such that the resulting nonlinear controller is guaranteed stable for the SMA ATVA system. Further, the modifications have the beneficial effect of permitting the use of higher-gain controllers. Experiments were performed using the nonlinear controllers and results are presented to demonstrate the improved performance that can be attained.

2. Closed-loop system model

2.1. Control goal

In previous work, Williams et al. [2] described the development and modeling of an SMA ATVA composed of NiTi (Nitinol) SMA beams embedded in an end-mass. The elastic modulus of NiTi varies with temperature, such that heating and cooling of the SMA beams is used to adapt the SMA ATVA stiffness, with corresponding changes in the SMA ATVA natural frequency. The basic open-loop plant is shown in Fig. 2. System inputs are the ambient temperature, T_∞, and the squared-current from a DC power supply, i^2. Those inputs map to an SMA beam temperature, x_T, through the temperature dynamics. In turn, x_T maps to an equivalent absorber stiffness, $k_a(x_T)$ which, in combination with ω_{exc}, determines the error signal $\cos(\phi_{\text{rel}})$ through the function $f(k_a, \omega_{\text{exc}})$. The role of the feedback controller is to control current to the SMA beams such that x_T will result in the appropriate tuned condition of the ATVA, as indicated by $\cos(\phi_{\text{rel}}) = 0$. It is acknowledged that online variation of the absorber stiffness, k_a, results in a time-varying system.

Fig. 2. Open-loop SMA ATVA system [2].

However, as noted in the work by Williams et al. [2], the separation between the temperature dynamics and the actual excitation frequency, ω_{exc}, is sufficiently large as to neglect the time-varying nature of the system. For example, for the system used in this work, the thermal time constants are on the order of multiple seconds, while ω_{exc} is above 40 Hz.

As noted above, the SMA element temperature x_T dictates the value of the error signal $\cos(\phi_{\mathrm{rel}})$ for a given ω_{exc}. The temperature dynamics are assumed to be first-order with a corresponding time constant τ. The gain between the squared-current input u and the steady-state temperature above T_∞ is k_T. The temperature dynamics are thus represented by the equation

$$\dot{x}_T = -\frac{1}{\tau}(x_T - T_\infty) + \frac{k_T}{\tau}\cdot u.$$

If the equilibrium temperature, x_{eq}, is defined as the specific x_T necessary to achieve $\cos(\phi_{\mathrm{rel}}) = 0$, then the model is simplified by introducing the perturbed temperature $\tilde{x} = x_T - x_{\mathrm{eq}}$. $\tilde{x}$ is thus the temperature difference between the instantaneous SMA beam temperature and the equilibrium beam temperature necessary to produce $\cos(\phi_{\mathrm{rel}}) = 0$. The dynamics for $\tilde{x}$ are described by the equation

$$\dot{\tilde{x}} = -\frac{1}{\tau}\cdot\tilde{x} + \frac{k_T}{\tau}\cdot u - \frac{1}{\tau}(x_{\mathrm{eq}} - T_\infty).$$

For the case of an absorber mounted on a primary system, the transfer function relating the primary system acceleration to the absorber acceleration is

$$\frac{s^2X_a(s)}{s^2X_P(s)} = \frac{c_a s + k_a(\tilde{x})}{m_a s^2 + c_a s + k_a(\tilde{x})},$$

where the absorber mass, damping, and stiffness are given by m_a, c_a, and $k_a(\tilde{x})$, respectively, $X_a(s)$ and $X_p(s)$ are the Laplace transforms of the absorber and primary system displacement, and s is the standard Laplace operator. The notation $k_a(\tilde{x})$ is used for the absorber stiffness to highlight its dependency on the SMA element temperature. Given the above transfer function, the phase relationship between the absorber and primary system vibration is governed by the relation

$$f(k_a(\tilde{x}),\omega_{\mathrm{exc}}) = \tan(\phi_{\mathrm{rel}}) = \frac{-c_a\cdot m_a\cdot\omega_{\mathrm{exc}}^3}{k_a^2(\tilde{x}) - k_a(\tilde{x})\cdot m_a\cdot\omega_{\mathrm{exc}}^2 + c_a^2\cdot\omega_{\mathrm{exc}}^2}.$$

After some trigonometric manipulation, the following expression for $\cos(\phi_{\mathrm{rel}})$ is obtained:

$$\cos(\phi_{\mathrm{rel}}) = \sqrt{\frac{1}{1+f^2(k_a(\tilde{x},\omega_{\mathrm{exc}}))}}.$$

By combining the temperature dynamics and the derivation for $\cos(\phi_{\mathrm{rel}})$, the overall system description is given by

$$\dot{\tilde{x}} = -\frac{1}{\tau}\cdot\tilde{x} + \frac{k_T}{\tau}\cdot u - \frac{1}{\tau}(x_{\mathrm{eq}} - T_\infty),$$

$$y = \cos(\phi_{\mathrm{rel}}(k_a(\tilde{x}))) = \begin{cases} \sqrt{\dfrac{1}{1+f^2(k_a(\tilde{x}),\omega_{\mathrm{exc}})}}, & f(k_a(\tilde{x}),\omega_{\mathrm{exc}})<0, \\ -\sqrt{\dfrac{1}{1+f^2(k_a(\tilde{x}),\omega_{\mathrm{exc}})}}, & f(k_a(\tilde{x}),\omega_{\mathrm{exc}})>0. \end{cases} \tag{1}$$

The only relationship not included in Eq. (1) is the mapping between the SMA element temperature and the resulting absorber stiffness $k_a(\tilde{x})$. That map can be obtained experimentally and curve-fits can be used to represent the map. An experimentally determined plot of $k_a(x_T)$ is shown in Fig. 3, along with different curve-fits described in Williams et al. [2].

The goal of the tuning problem is to achieve the condition $\tilde{x} = 0$. Thus, it would seem that the problem is one of temperature control. However, $\tilde{x}$ is not directly measurable and the output, $y = \cos(\phi_{\mathrm{rel}})$, is measurable. For a fixed ω_{exc}, the relationship between $\tilde{x}$ and y is unique. This is due to the unique mapping between $\cos(\phi_{\mathrm{rel}})$ and ω_{abs} and the mapping between $\tilde{x}$ and k_a, as shown in Figs. 1 and 3, respectively. The two mappings may be combined into a single mapping that relating $\tilde{x}$ to $\cos(\phi_{\mathrm{rel}})$. As shown in Fig. 4, that mapping is a strictly increasing function in the first and third quadrants. The strictly increasing nature of the relationship between $\tilde{x}$ and y will be instrumental in determining the stability of the system for different controllers.

2.2. Controller structure

Steady state power is required to maintain x_{eq}, even in the case where $\cos(\phi_{\mathrm{rel}}) = 0$. As such, integral action is necessary in the controller. A PI controller is a logical starting point for

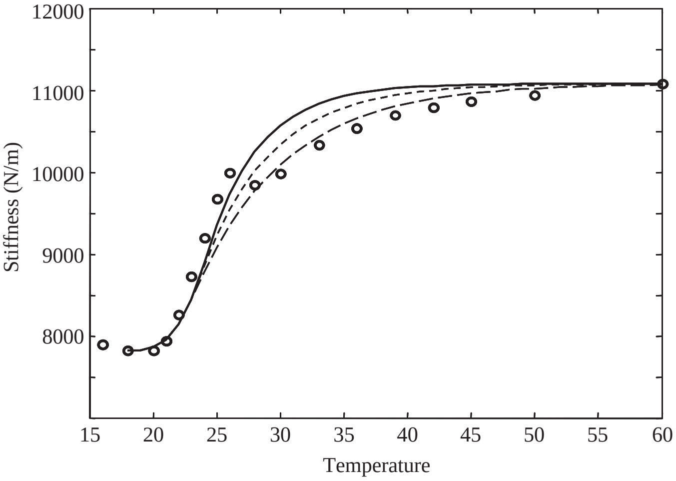

Fig. 3. SMA ATVA stiffness vs. temperature. ○ experimental, —— curve fit 1, - - - curve fit 2, –·– curve fit 3.

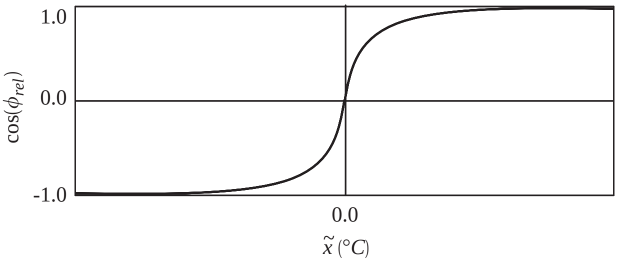

Fig. 4. Sketch of $\cos(\phi_{\text{rel}})$.

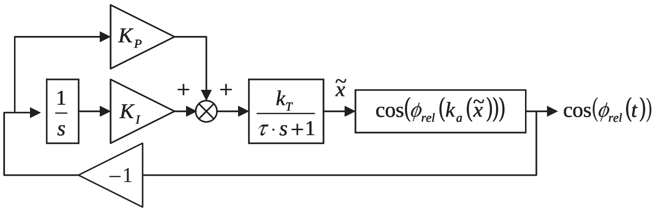

Fig. 5. Closed-loop SMA ATVA system.

controller design. With the error signal $\cos(\phi_{\text{rel}})$, the basic form of the PI controller is

$$u = -K_P \cos(\phi_{\text{rel}}) - K_I \int_0^t \cos(\phi_{\text{rel}})\,\mathrm{d}t,$$

where K_P and K_I are the proportional and integral controller gains, respectively. In that expression, the signs on the two controller terms are both negative. This is because the feedback signal from the system output is $\cos(\phi_{\text{rel}})$ and the reference value from the input is 0. If the integral of $\cos(\phi_{\text{rel}})$ is defined as a second state x_I, then the control law is rewritten as

$$u = -K_P \cdot \dot{x}_I - K_I \cdot x_I. \tag{2}$$

Using Eq. (2) to close the feedback loop results in the second-order closed-loop system shown in Fig. 5 and the state equations

$$\begin{aligned} \dot{\tilde{x}} &= -\frac{1}{\tau}\cdot\tilde{x} - \frac{k_T \cdot K_P}{\tau}\cos(\phi_{\text{rel}}(\tilde{x})) - \frac{k_T \cdot K_I}{\tau} x_I - \frac{1}{\tau}(x_{\text{eq}} - T_\infty), \\ \dot{x}_I &= \cos(\phi_{\text{rel}}(\tilde{x})) = \begin{cases} \sqrt{\dfrac{1}{1 + f^2(k_a(\tilde{x}), \omega_{\text{exc}})}}, & f(k_a(\tilde{x}), \omega_{\text{exc}}) < 0, \\ -\sqrt{\dfrac{1}{1 + f^2(k_a(\tilde{x}), \omega_{\text{exc}})}}, & f(k_a(\tilde{x}), \omega_{\text{exc}}) > 0. \end{cases} \end{aligned} \tag{3}$$

The challenge of selecting appropriate K_P and K_I values is addressed in the next section.

3. Linear controller design

As a first step in the design of a controller for the SMA ATVA, the system was linearized about the desired steady-state value $\tilde{x} = 0$ (equivalent to the condition $x_T = x_{\text{eq}}$) for a fixed excitation frequency of 42.7 Hz. In performing the linearization, three nonlinearities were considered: control effort saturation, stiffness saturation as shown in Fig. 3, and fact that the error signal $\cos(\phi_{\text{rel}})$ was limited to be within the bounds of ± 1. The control effort saturated at an upper bound given by the maximum squared-current of the DC power supply, $i^2_{\max}$, and at a lower bound of $i^2_{\min} = 0$, as active cooling was not used in this effort. The stiffness saturation and the bounds on $\cos(\phi_{\text{rel}})$ were lumped into a single static nonlinearity $\cos(\phi_{\text{rel}}(\tilde{x}))$, as described previously and shown in Fig. 4. $\cos(\phi_{\text{rel}})$ is approximately -1 for temperatures significantly below x_{eq} and increases to $+1$ over a very narrow range of temperatures about x_{eq}. To examine this behavior, an SMA ATVA was implemented on a primary system as shown in Fig. 6. The physical dimensions of the SMA ATVA and the primary system are shown in Tables 1 and 2. The primary system was excited with a 42.7 Hz signal. After 30 s, a squared-current of approximately 53 A^2 was passed through the SMA beam elements for 360 s. The current was then removed and the test continued for an additional 330 s. The resulting plot of SMA beam temperature is shown in Fig. 7 and the corresponding plots of primary mass acceleration and $\cos(\phi_{\text{rel}})$ are shown in Fig. 8.

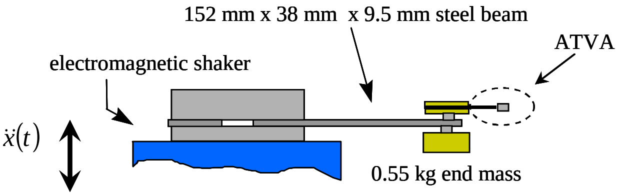

Fig. 6. SMA ATVA and primary system mounted on a shaker.

Table 1
SMA ATVA dimensions

r_{steel}	1.06 mm
r_{SMA}	1.22 mm
L	60 mm
M_{end}	0.132 kg
m_{beam}	0.00724 kg

Table 2
Primary system dimensions

b_b	38 mm
h_b	9.5 mm
L	152 mm
M_{end}	0.55 kg
m_{beam}	1 kg

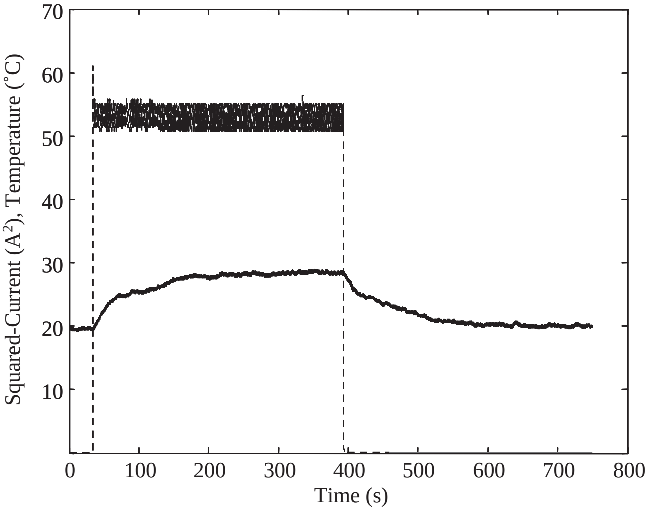

Fig. 7. SMA beam current and temperature during test: - - -, squared-current; ——, temperature.

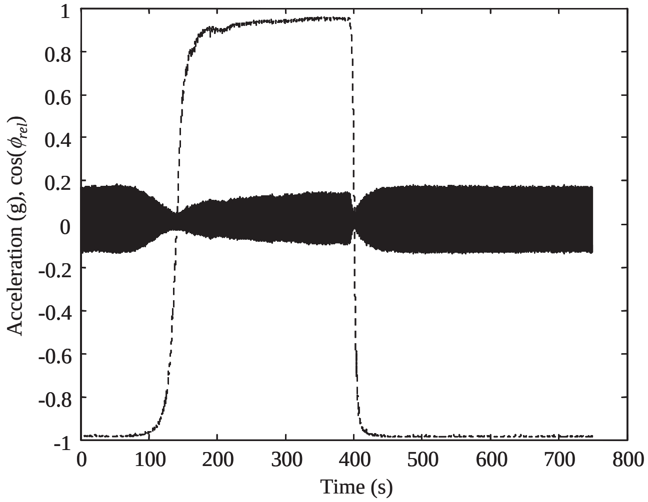

Fig. 8. Primary mass acceleration and $\cos(\phi_{\mathrm{rel}})$ during test: ——, acceleration; - - -, $\cos(\phi_{\mathrm{rel}})$.

$\cos(\phi_{\mathrm{rel}})$ was then plotted as a function of x_T as shown in Fig. 9. In that figure, two curves are apparent. The curve on the right is the plot of $\cos(\phi_{\mathrm{rel}})$ vs. x_T during the cooling phase, while the left curve is the same plot during the heating phase. As noted by Williams et al. [2], any hysteresis in the curves is relatively insignificant and is attributed more to the difficulty of obtaining precise temperature measurements with the SMA elements vibrating in open laboratory air.

To linearize the system about x_{eq}, $\cos(\phi_{\mathrm{rel}}(\tilde{x}))$ is modeled as a static gain equal to the slope of the $\cos(\phi_{\mathrm{rel}})$ vs. x_T curve as it passes $\cos(\phi_{\mathrm{rel}}) = 0$. This substitution is shown in Fig. 10. If the static gain is defined as k_c, then for deviations about the $\cos(\phi_{\mathrm{rel}}) = 0$ operating point, the system

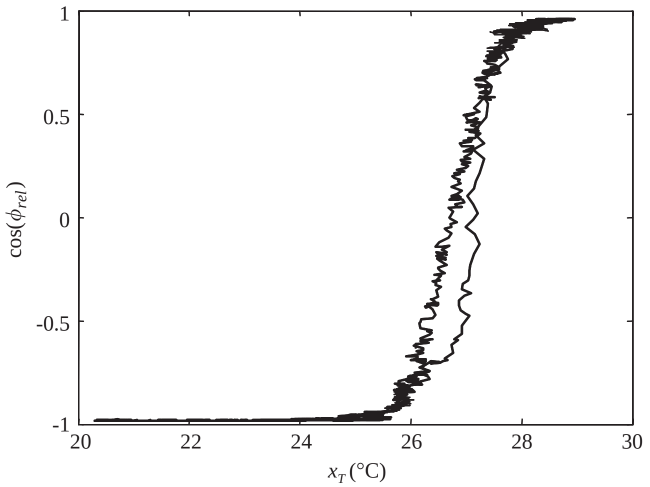

Fig. 9. $\cos(\phi_{\mathrm{rel}})$ as a function of SMA beam temperature.

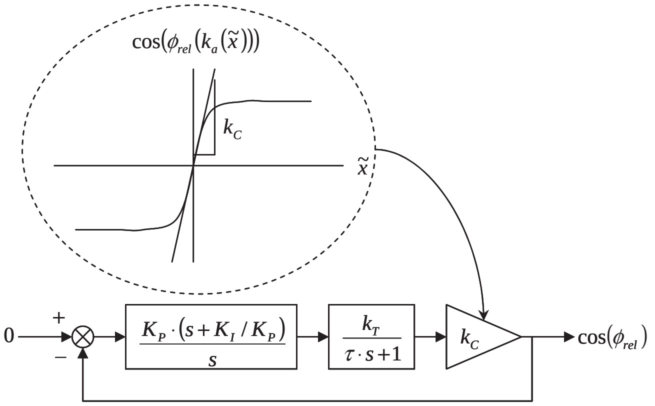

Fig. 10. Linearized closed-loop SMA ATVA system.

dynamics are approximately modeled by the transfer function

$$G(s)=\frac{\frac{K_P\cdot k_T\cdot k_C}{\tau}(s+K_I/K_P)}{s^2+\left(\frac{1+K_P\cdot k_T\cdot k_C}{\tau}\right)\cdot s+\frac{K_P\cdot k_T\cdot k_C}{\tau}(K_I/K_P)}. \tag{4}$$

The output of $G(s)$ is $\cos(\phi_{\mathrm{rel}})$, while the input is the reference value $\cos(\phi_{\mathrm{rel}})=0$.

In a standard linear control problem, K_P and K_I could be chosen to provide a certain system bandwidth and damping. In the case of the SMA ATVA, however, use of the spring stiffness k_C is only valid in a very narrow region about x_{eq}. Outside of that region, k_C drops to a small value. A controller designed according to the value of k_C in the vicinity of x_{eq} will provide a potentially sluggish response at other values of x_T. Conversely, if the controller is designed according to the value of k_C far from x_{eq}, the plant gain will become large near x_{eq} and significant overshoot would occur. As a starting point, the proportional gain K_P was chosen such that the controller would saturate for a maximum error of $\cos(\phi_{\mathrm{rel}}) = 1.0$. That value of K_P produces the largest range of linear operation about x_{eq}, while still providing for the widest range of control signals. A larger K_P would cause saturation at smaller values of $\cos(\phi_{\mathrm{rel}})$ and contract the range of linear operation. At the same time, a smaller K_P will never produce the maximum control effort, because $\cos(\phi_{\mathrm{rel}})$ is limited to the range $\cos(\phi_{\mathrm{rel}}) \in (-1, 1)$. To calculate the value of K_P such that the controller reaches the saturation state, the following procedure was used:

(1) Determine the equilibrium temperature, x_{eq}, for a given excitation. From Fig. 8, $x_{\mathrm{eq}} = 26.5\,^{\circ}\mathrm{C}$ for the 42.7 Hz excitation.
(2) Determine the squared-current, i^2_{eq}, required to maintain x_{eq} at a given ambient temperature using x_{eq} and the gain of the temperature dynamics, k_T. An approximate $k_T = 0.2\,^{\circ}\mathrm{C}/\mathrm{A}^2$ was determined from open-loop temperature testing. k_T was used together with an assumed $T_\infty = 22\,^{\circ}\mathrm{C}$ to estimate $i^2_{\mathrm{eq}} = 22\ \mathrm{A}^2$.
(3) Determine the "nearest" saturation; either at $i^2_{\max}$ with an error of $\cos(\phi_{\mathrm{rel}}) = +1.0$ or at $i^2_{\min} = 0\ \mathrm{A}^2$ with an error of $\cos(\phi_{\mathrm{rel}}) = -1.0$. With a power supply limit of 10 A, saturation at $i^2_{\min} = 0\ \mathrm{A}^2$ was the nearest saturation.
(4) If $(i^2_{\max} - i^2_{\mathrm{eq}}) < i^2_{\mathrm{eq}}$, then the system will saturate at the maximum control effort first. For this case, K_P is equal to $(i^2_{\max} - i^2_{\mathrm{eq}})$. Otherwise, the system will saturate at zero current first. For this case set $K_P = i^2_{\mathrm{eq}}$. As noted previously, saturation at $0\,\mathrm{A}^2$ was anticipated, so $K_P = 22\,\mathrm{A}^2$.

Once K_P is chosen, K_I was calculated to provide the linearized system with a damping ratio $\zeta = 0.707$. Based on the data shown in Fig. 9 and data from other similar tests, k_C estimates were bounded by $k_C|_{\min} = 1.33\,^{\circ}\mathrm{C}^{-1}$ to $k_C|_{\min} = 8\,^{\circ}\mathrm{C}^{-1}$. Using the values of k_T, τ, K_P, and ζ, the corresponding range of K_I values are $K_I|_{\min} = 1.5\ \mathrm{A}^2/\mathrm{s}$ and $K_I|_{\min} = 13\ \mathrm{A}^2/\mathrm{s}$. The broad range of K_I reflects the fact that a range of x_{eq} are obtained for the different excitation frequencies. For this set up, the range of x_{eq} is broad, when compared to the nominal beam temperature above ambient, such that the temperature dynamics varied across the range of potential SMA temperatures.

To test the controller, the shaker was driven at 41 Hz with an amplitude of 0.2 g. ω_{exc} was then stepped up to 42.5 Hz, up to 44 Hz, down to 42.5 Hz, and finally back to 41 Hz. Accelerometers mounted on the primary mass and on the absorber mass were used to measure the acceleration data that was used to determine $\cos(\phi_{\mathrm{rel}})$. For the first 30 s of testing, no error signal was passed to the controller, to allow the system to come to a steady state. After 30 s, the value of $\cos(\phi_{\mathrm{rel}})$ was provided to a PI controller. The controller gains were $K_P = 22\,\mathrm{A}^2$ and $K_I = 1.52\,\mathrm{A}^2/\mathrm{s}$. The lower value of K_I was chosen for the first tests to minimize the potential for integrator windup. The experimental results are shown in Fig. 11, which contains plots of the primary mass acceleration, $\cos(\phi_{\mathrm{rel}})$, and the current running through the SMA beam elements during the test. The primary mass acceleration is also plotted for the case of no ATVA implemented, to demonstrate the improved vibration performance obtained when implementing the ATVA.

As shown in Fig. 11, the controller drives $\cos(\phi_{\mathrm{rel}})$ to zero after each step change in ω_{exc}. At the same time, the acceleration response of the primary system is significantly reduced. For clarity's

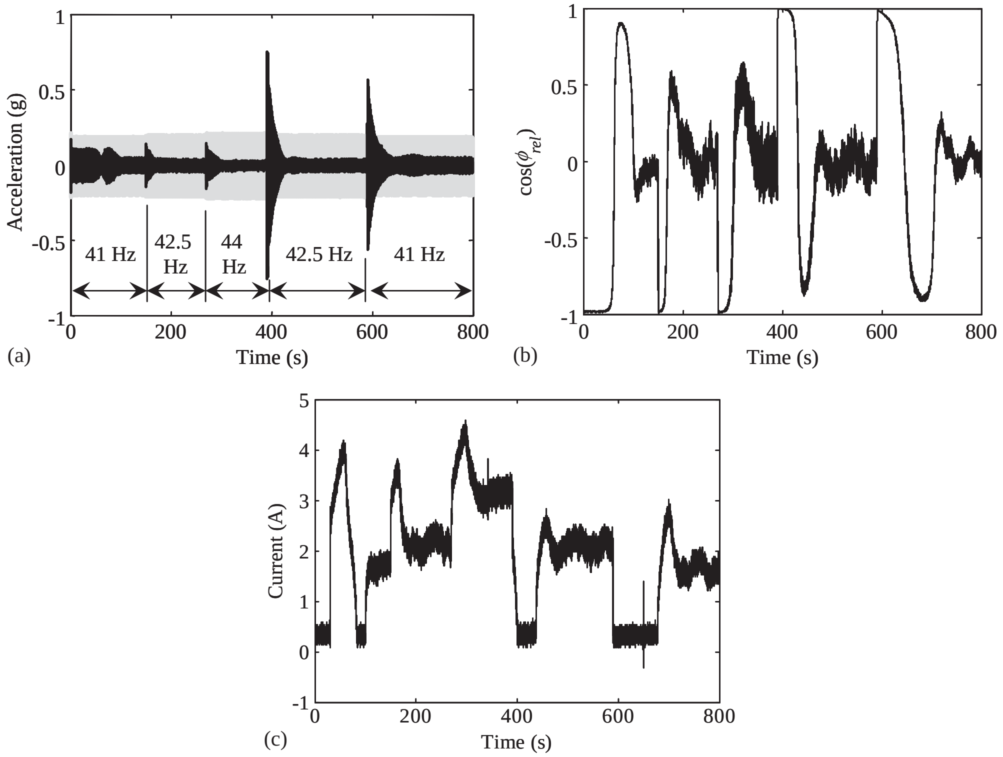

Fig. 11. SMA ATVA system response to step changes in excitation frequency, $K_P = 22$, $K_I = 1.52$, (a) primary mass acceleration, □, no absorber; ■, controlled SMA ATVA; (b) cosine of relative phase; (c) control current.

sake, the response to the 41 Hz excitation is shown in Fig. 12 and the response to the step down from 42.5 to 41 Hz is shown in Fig. 13. The reason for the large amplitude of the primary mass acceleration just after the step down to 41 Hz is that the 42.5 Hz tuned condition of the absorber introduces a 41 Hz resonance in the frequency response of the primary system. As a consequence, the sudden step down to 41 Hz is actually a step down to a resonant condition that goes away as the controller appropriately tunes the absorber.

In both Figs. 12 and 13, overshoot is also apparent in the system response. In Fig. 12, the system attains $\cos(\phi_{\mathrm{rel}}) = 0$ in a very short time; at approximately 60 s into the test, which is only 30 s after the start of control. However, windup in the integrator results in continued heating of the SMA elements such that steady-state operation near $\cos(\phi_{\mathrm{rel}}) = 0$ is not attained until much farther into the test. As a consequence, the primary mass acceleration at first decreases as the appropriate tuning is achieved and then increases due to the overshoot, as can be seen in the "hump" in the acceleration response shown in Fig. 12. The penalty for the overshoot in the "tuning down" case is not as apparent, although it still occurs, as shown in Fig. 13.

In general, overshoot is not desirable, but in the case of an ATVA, it can be particularly problematic, as overshoot of the target-tuned condition may result in excitation of the primary system at resonance. In the case of the SMA ATVA, a large contributor to the overshoot is the saturation of the control effort at $i^2_{\min} = 0$. With the nonlinearity of $\cos(\phi_{\mathrm{rel}}(\tilde{x}))$ and the hard

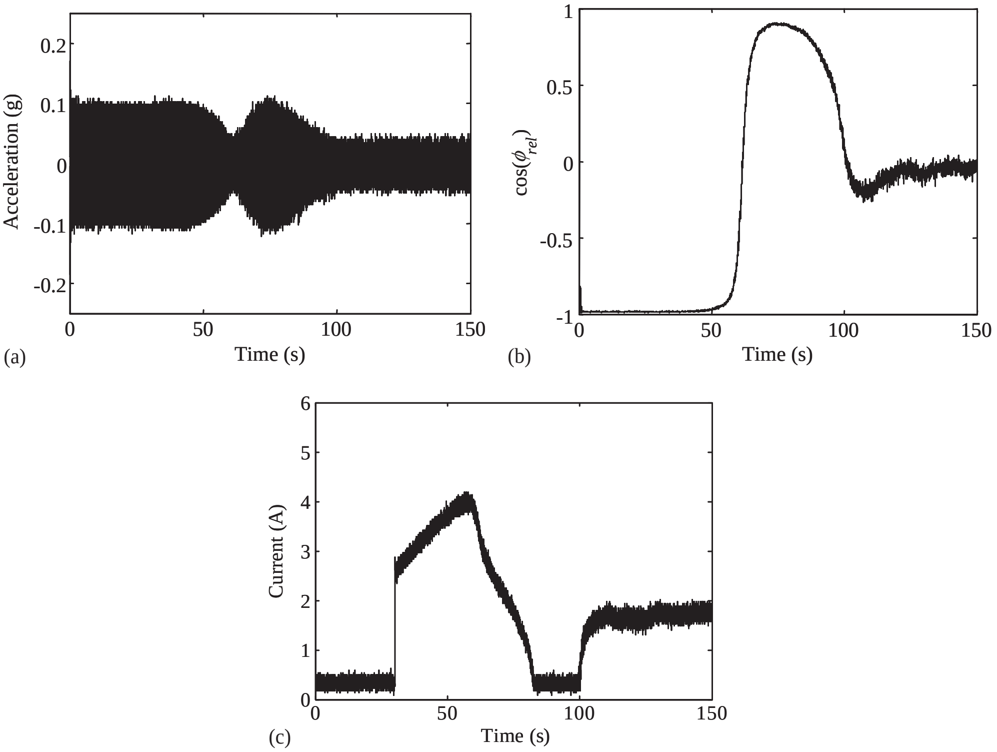

Fig. 12. System response to 41 Hz excitation, starting from zero error at 30 s, $K_P = 22$, $K_I = 1.52$. (a) Primary mass acceleration, (b) cosine of relative phase, (c) control current.

saturation due to the controller effort limitations, it is reasonable to consider if the system can be driven unstable. While the experimental results indicate that it is possible to use $\cos(\phi_{\text{rel}})$ as an error signal, it is important to determine if the current control scheme is stable or if a controller can be designed that results in a stable closed-loop system. In the next section of this work, the stability of the SMA ATVA system is investigated.

4. System stability and nonlinear controller design

4.1. Stability in the absence of control saturation

For the purposes of this work, stability of the SMA ATVA system refers to the guarantee that the SMA ATVA will attain the condition $\cos(\phi_{\text{rel}}) = 0$. This is achieved by driving the state $\tilde{x}$ to zero and driving the state x_I to the value such that the current passing through the SMA elements is sufficient to maintain the SMA element temperature at x_{eq}. As a first step for investigating stability, controller saturation was ignored. With the nonlinear function $\cos(\phi_{\text{rel}}(\tilde{x}))$, a standard linear analysis is not possible and a Lyapunov stability analysis was performed. The first step was to choose a candidate Lyapunov function that is positive definite for all possible system states. If the derivative of that function is negative definite, then the system is stable. In the system

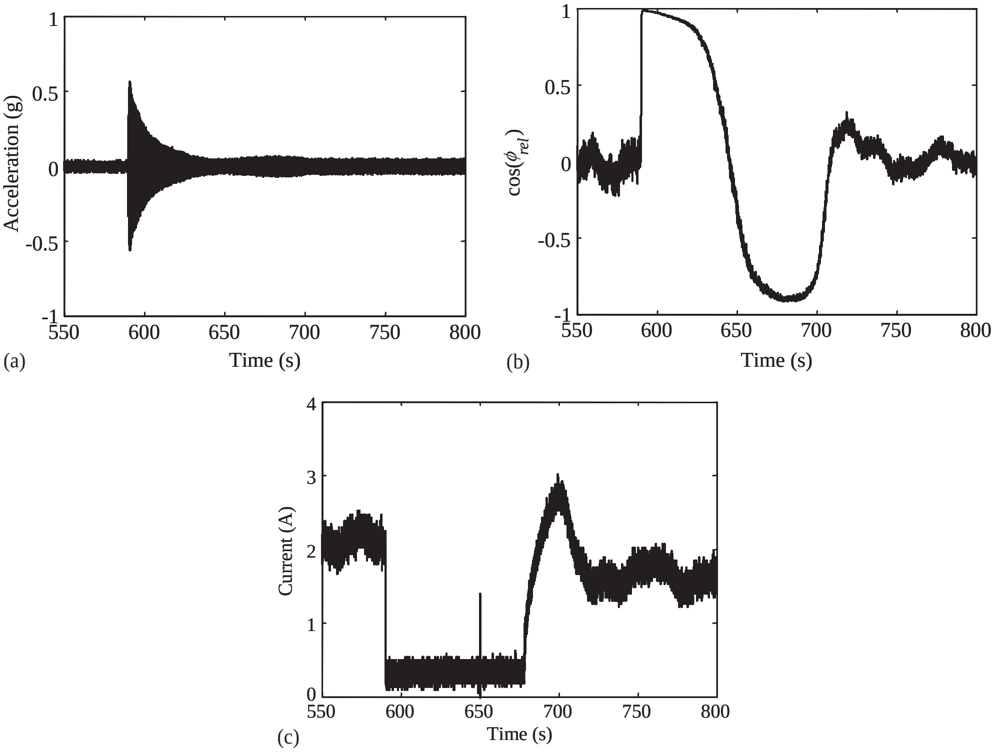

Fig. 13. System response to step from 42.5 to 41 Hz excitation $K_P = 22$, $K_I = 1.52$. (a) Primary mass acceleration, (b) cosine of relative phase, (c) control current.

description of Eq. (3), the system state vector is $[x_I, \tilde{x}]^{\mathrm{T}}$. Using those states, the Lyapunov function chosen for the analysis is

$$V(x_I, \tilde{x}) = \frac{K_I \cdot k_T}{2 \cdot \tau}\left(x_I + \left(\frac{x_{\mathrm{eq}} - T_\infty}{K_I \cdot k_T}\right)\right)^2 + \int_0^{\tilde{x}} \cos(\phi_{\mathrm{rel}}(\eta))\,\mathrm{d}\eta. \tag{5}$$

The squared term in Eq. (5) is always positive if $K_I > 0$. The integral term is also always positive, as the signs of $\cos(\phi_{\mathrm{rel}}(\eta))$ and $\mathrm{d}\eta$ are always the same. Thus $V(x_I, \tilde{x})$ is always greater than or equal to zero. $V(x_I, \tilde{x})$ will only be equal to zero if each of the terms in Eq. (5) are identically zero. The second term is zero only if $\tilde{x} = 0$. The first term is only zero if $K_I \cdot k_T \cdot x_I = (x_{\mathrm{eq}} - T_\infty)$. The squared-current passing through the SMA elements is $K_I \cdot x_I$ and k_T is the gain between the squared-current and SMA element temperature above T_∞. As such, $K_I \cdot k_T \cdot x_I = (x_{\mathrm{eq}} - T_\infty)$ implies that the SMA element temperature is maintained at the desired equilibrium temperature x_{eq}. Hence, $V(x_I, \tilde{x})$ is positive definite, provided $K_I > 0$. The time derivative of Eq. (5) is

$$\begin{aligned} \dot{V}(x_I, \tilde{x}) &= \frac{K_I \cdot k_T}{\tau} \cdot x_I \cdot \dot{x}_I + (x_{\mathrm{eq}} - T_\infty)\dot{x}_I + \cos(\phi_{\mathrm{rel}}(\tilde{x}))\dot{\tilde{x}} \\ &= -\frac{k_T}{\tau} \cdot K_P \cdot \dot{x}_I^2 - \frac{1}{\tau} \cdot \tilde{x} \cdot \dot{x}_I. \end{aligned} \tag{6}$$

In Eq. (6), the first term is zero only if $\dot{x}_I = 0$ and is negative for all other $\dot{x}_I$. $\tilde{x}$ and $\dot{x}_I$ always have the same sign, as shown in Fig. 4, such that the second term in Eq. (6) is negative for all non-zero $\tilde{x}$ and $\dot{x}_I$. The second term is zero when either $\tilde{x}$ or $\dot{x}_I$ is zero. As such, $\dot{V}(x_I, \tilde{x})$ is negative definite and the system is stable in the absence of control saturations.

Without active cooling, control saturations are likely if ω_{exc} drops suddenly. Depending on the power supply current limits and the size of step increases of ω_{exc}, heating saturation may be an issue as well. As noted previously, the control effort u is a linear function of x_I and $\dot{x}_I$: $u = -K_P \cdot \dot{x}_I + K_I \cdot x_I$. Given that control signal, controller saturations are thus lines in the $\{x_I, \dot{x}_I\}$ phase plane. That is, control saturations occur along the lines $u_{\max} = -K_P \cdot \dot{x}_I + K_I \cdot x_I$ and $u_{\min} = -K_P \cdot \dot{x}_I + K_I \cdot x_I$. For this reason, the stability analysis is somewhat simplified if the system is examined in the $\{x_I, \dot{x}_I\}$ phase plane. This is a valid approach, as the variables $\tilde{x}$ and $\dot{x}_I$ are related by a nonlinear coordinate transformation as shown in Fig. 4. Defining that transformation according to $\dot{x}_I = N(\tilde{x})$, $N(\tilde{x})$ is strictly increasing, is always in the first and third quadrants, and passes through the origin. The inverse transformation $\tilde{x} = N^{-1}(\dot{x}_I)$ also exists, for $-1 \leqslant \dot{x}_I \leqslant 1$, such that the system dynamics can be expressed by the nonlinear second-order differential equation

$$\ddot{x}_I = \frac{\partial N(\tilde{x})}{\partial \tilde{x}} \cdot \dot{\tilde{x}} = \frac{\partial N(\tilde{x})}{\partial \tilde{x}} \left[-\frac{1}{\tau} \cdot N^{-1}(\dot{x}_I) - \frac{K_P \cdot k_T}{\tau} \cdot \dot{x}_I - \frac{K_I \cdot k_T}{\tau} \cdot x_I - \frac{1}{\tau}(x_{\text{eq}} - T_\infty) \right]. \quad (7)$$

Further, as also shown in Fig. 4, driving $\tilde{x}$ to zero implies that $\dot{x}_I$ also goes to zero. As such, it is sufficient to consider system stability in the $\{x_I, \dot{x}_I\}$ phase plane. While the expression in Eq. (7) is not directly implemented in the stability analysis, it is used to demonstrate that analysis of the system using the state vector $[x_I, \dot{x}_I]^{\mathrm{T}}$ is equivalent to analysis of the system using the state vector $[x_I, \tilde{x}]^{\mathrm{T}}$.

By defining the maximum and minimum control efforts as $u_{\max} = i^2_{\max}$ and $u_{\min} = 0$, the $\{x_I, \dot{x}_I\}$ phase plane is separated into saturated and unsaturated regions as shown in Fig. 14. An $\dot{x}_I$ vs. x_I phase portrait was plotted using data from the initial 41 Hz excitation response shown in Fig. 12 and is shown superimposed over the saturation boundaries in Fig. 14. As shown in Fig. 14, saturation during the heating phase does not occur. In the cooling range, the system saturates in the $u_{\min} = 0$ region for a period of time. That saturation is also apparent in the time plot of the current from approximately 80–100 s as shown in Fig. 12.

To further demonstrate the saturation behavior, the controller gains were increased to $K_P = 44$ and $K_I = 26$ and the system was excited with the same series of step changes in ω_{exc}. The system response to the 41 Hz excitation and the corresponding phase portrait are shown in Figs. 15 and 16, respectively. In Fig. 16, the system appear stables and it may be reasonable to expect that given enough time, the trajectory would converge to a steady solution $\cos(\phi_{\text{rel}}) = 0$. However, there is no guarantee that convergence will occur. As such, it is important to continue the analysis and determine stability for the general case. To that end, the Lyapunov analysis was extended to include controller saturations.

4.2. Stability in the presence of saturation

If controller saturations are included in the analysis, the system's response is dictated by three different sets of dynamics. In the unsaturated region, the dynamics described by Eq. (3) are valid.

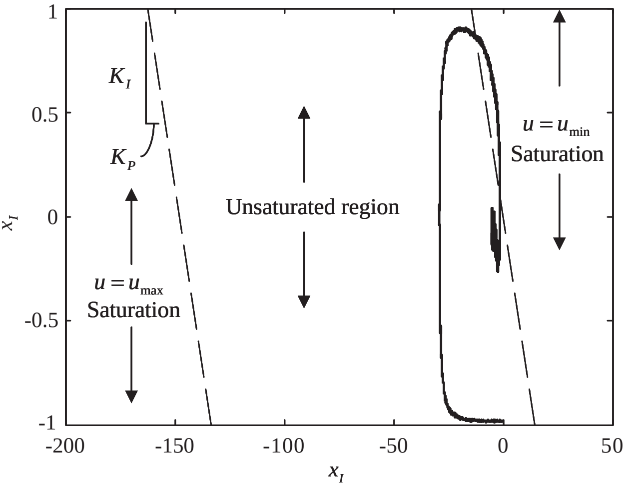

Fig. 14. Saturation boundaries in the $(x_I, \dot{x}_I)$ plane superimposed over phase portrait of SMA ATVA response to 41 Hz excitation, zero initial conditions, $K_P = 22$, $K_I = 1.52$.

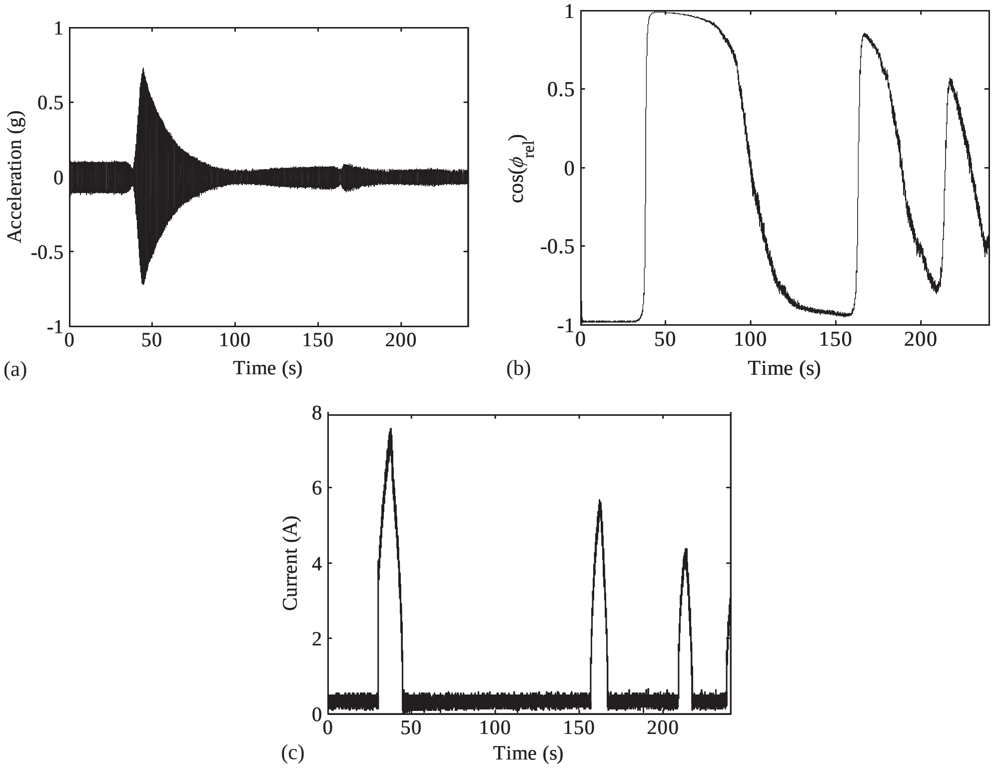

Fig. 15. SMA ATVA system response to 41 Hz excitation, $K_P = 44$, $K_I = 26$. (a) Primary mass acceleration, (b) cosine of relative phase, (c) control current.

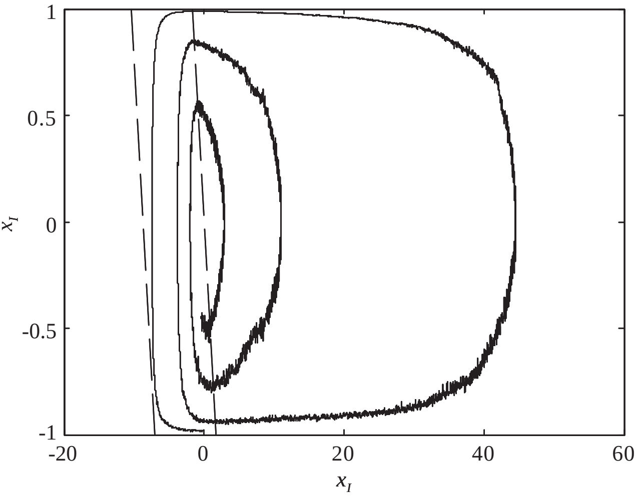

Fig. 16. Phase portrait for system response shown in Fig. 15.

In the saturated regions, the system dynamics are determined by using $u = u_{\max} = i^2_{\max}$ and $u = u_{\min} = 0$. If those control signals are substituted for the linear PI controller originally represented by Eq. (2), the corresponding Lyapunov function derivatives are

$$\dot{V}(u_{\min}) = \frac{K_I \cdot k_T}{\tau} \cdot x_I \cdot \dot{x}_I - \frac{1}{\tau} \cdot \tilde{x} \cdot \dot{x}_I \tag{8}$$

and

$$\dot{V}(u_{\max}) = \frac{K_I \cdot k_T}{\tau} \cdot x_I \cdot \dot{x}_I - \frac{1}{\tau} \cdot \tilde{x} \cdot \dot{x}_I + \frac{k_T}{\tau} \cdot u_{\max} \cdot \dot{x}_I. \tag{9}$$

From Eqs. (8) and (9), there will be regions in the $\{x_I, \dot{x}_I\}$ plane where $\dot{V}(x_I, \dot{x}_I) > 0$. In Eq. (8), for example, the second term is always negative, as $\dot{x}_I$ and $\tilde{x}$ always have the same sign. In the first and third quadrants, however, the first term is always positive. As such, at any fixed location in the first and third quadrants, $\dot{V}(x_I, \dot{x}_I)$ can be made larger than zero by increasing K_I sufficiently. For a fixed K_I, therefore, there are locations in the first and third quadrants where $\dot{V}(x_I, \dot{x}_I) > 0$. The locations and general shape of those regions are shown in Fig. 17. Following the above analysis, the size of the $\dot{V}(x_I, \dot{x}_I) > 0$ regions increases with increasing K_I.

Because of the existence of the $\dot{V}(x_I, \dot{x}_I) > 0$ regions, the Lyapunov analysis is inconclusive with respect to system stability. To further continue the analysis requires either the determination of a different candidate Lyapunov function $V(x_I, \dot{x}_I)$ or a modification of the system dynamics to avoid the $\dot{V}(x_I, \dot{x}_I) > 0$ regions. The latter approach was taken and the controller was modified to ensure that the system trajectories remained in the $\dot{V}(x_I, \dot{x}_I) < 0$ regions. To achieve that effect, reset action was used with the state variable x_I. $\dot{x}_I = \cos(\phi_{\text{rel}})$ is a measured physical quantity and cannot be modified. x_I, however, is a numerical quantity internal to the controller and can be reset arbitrarily. To take advantage of this, the controller was changed to allow for resetting x_I when saturation of the control effort is detected. For example, in a cooling phase, if a negative

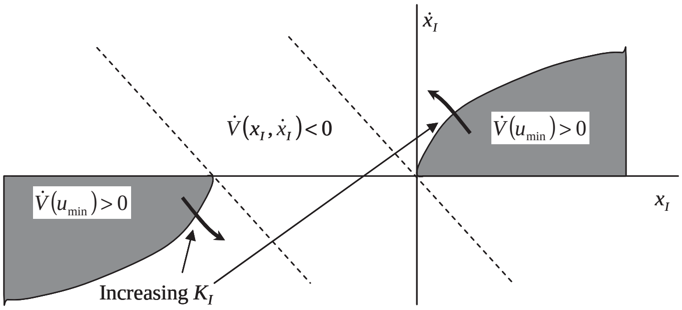

Fig. 17. $\dot{V}(x_I, \dot{x}_I)$ characteristics in the (x_I, x_I) plane.

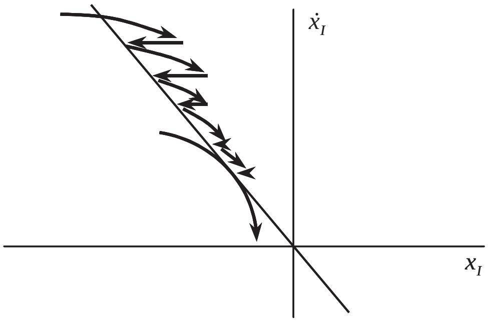

Fig. 18. Reset of x_I to avoid saturation.

squared-current is requested, x_I is reset to a value such that the controller requests $u_{\min} = 0\,\mathrm{A}^2$. This reset action is shown in Fig. 18.

The reset value of x_I is determined based on the particular saturation boundary and the instantaneous value of $\dot{x}_I$. The $u_{\min} = 0\,\mathrm{A}^2$ saturation boundary is described by the equation

$$\dot{x}_I = -\frac{K_P}{K_I} \cdot x_I.$$

Using that relation, the reset value of x_I is

$$x_I = -\frac{K_I}{K_P} \cdot \dot{x}_I. \tag{10}$$

In a similar fashion, along the $u_{\max} = i^2_{\max}\,\mathrm{A}^2$ saturation boundary, the reset equation is

$$x_I = -\left(\frac{u_{\max} + K_P \cdot \dot{x}_I}{K_I}\right). \tag{11}$$

For implementation of this controller, the calculated control output is examined before modifying the controller output at each time-step. If the controller is requesting a negative output, x_I is reset according to Eq. (10). If the controller is requesting an output greater than $u_{\max}$, then x_I is reset according to Eq. (11). The logic is simple and easily implemented.

5. Stability of the nonlinear controller

To examine the stability of the SMA ATVA system with the modified controller, the $\{x_I, \dot{x}_I\}$ plane was split into three distinct regions as shown in Fig. 18: region (A) where no controller saturation occurs and regions (B) and (C), where the controller saturates at $u_{\min}$ and $u_{\max}$, respectively. The role of the controller is to drive all possible system trajectories to the equilibrium position $[x_I, \dot{x}_I]^{\mathrm{T}} = [-u_{ss}/K_I, 0]$, where u_{ss} is the steady state squared-current required to maintain x_{eq}. The necessary conditions for stability are first, the unsaturated region (A) is an attractive set for any trajectories starting outside of (A) and second, once within (A), all trajectories will approach the equilibrium position.

5.1. System behavior along the saturation boundaries

To show that (A) is an attractive set, trajectories starting within region (B) will be considered first. For all trajectories in (B), the reset action will immediately reset those trajectories to the (A)–(B) saturation boundary, such that it is sufficient to consider only trajectories starting along that boundary. Three characteristics of those trajectories must be described

(1) Along the (A)–(B) boundary all trajectories have $\ddot{x}_I < 0$, such that they are directed downward in the $\{x_I, \dot{x}_I\}$ plane.
(2) Along the (A)–(B) boundary, the trajectory slopes are near zero for $\ddot{x}_I$ close to 1.0 (at the top of the boundary). Moving down the boundary, the slopes are negative with increasing magnitude, such that at some point along the (A)–(B) boundary in the upper half-plane, the trajectory slopes become tangent to the trajectory boundary. That point is labeled t_{AB}.
(3) With the reset action, all trajectories along the (A)–(B) boundary above t_{AB} will "slide" down the boundary to t_{AB}, at which point they will enter the unsaturated region (A). All trajectories along the (A)–(B) boundary below t_{AB} will enter the unsaturated region (A) immediately.

To prove the first point, with $u_{\min} = 0$, the temperature dynamics of trajectories along the (A)–(B) boundary are be given by

$$\dot{\tilde{x}} = -\frac{1}{\tau} \cdot \tilde{x} - \frac{1}{\tau}(x_{eq} - T_\infty),$$

such that $\dot{\tilde{x}} \leqslant 0$ if $(-x_T + T_\infty) < 0$. As active cooling is not used in this work, it is impossible for x_T to be less than T_∞, and $\dot{\tilde{x}} \leqslant 0$ occurs. $\dot{\tilde{x}} = 0$ only occurs if the SMA beam element temperature equals the ambient temperature. In practice, such a situation will not occur, as the SMA ATVA will have been designed such that the minimum operating temperature is greater than T_∞. As such, $\dot{\tilde{x}} < 0$ along the (A)–(B) boundary. As shown in Fig. 4, $\mathrm{sgn}(\dot{\tilde{x}}) = \mathrm{sgn}(\ddot{x}_I)$, with the result that $\ddot{x}_I < 0$ for all trajectories along the (A)–(B) boundary and the first point is proven.

The slope of the trajectories is given by the ratio $m = \partial \dot{x}_I / \partial x_I$. Using the chain-rule, $m = \ddot{x}_I / \dot{x}_I$. Thus, as $\dot{x}_I = \cos(\phi_{\mathrm{rel}}) \to 1.0$, $m \to \ddot{x}_I$. Next, the chain rule is used expand $\ddot{x}_I$, such that $\ddot{x}_I = (\partial \dot{x}_I / \partial \tilde{x}) \dot{\tilde{x}}$. As $\dot{x}_I = \cos(\phi_{\mathrm{rel}}) \to 1.0$, $\partial \dot{x}_I / \partial \tilde{x} \to 0$, as shown in Fig. 4, such that $m \to 0$ as $\dot{x}_I \to 1.0$ toward the top of the (A)–(B) saturation boundary. As the trajectories "slide" down the (A)–(B) boundary, the trajectory slopes become progressively more negative until, at the crossing of the

x_I axis, $m = -\infty$. At some point during the progression from near-zero slopes down to negative infinite slopes, the trajectory slopes will be $-K_I/K_P$, the slope of the (A)–(B) boundary. That location is the previously described t_{AB} and thus, the second point is proven.

Finally, the reset action will force any trajectory starting in region (B) to be a point along the (A)–(B) boundary. For points reset to the boundary above t_{AB}, the trajectories will "attempt" to leave the boundary for the reasons described above. However, the reset action and the negative slopes will combine to force those trajectories to slide down to t_{AB}. At that point, the trajectories will enter region (A). Any points starting in (B) and reset to the (A)–(B) boundary below t_{AB} will enter region (A), as the slopes are more negative than the slope of the boundary. Thus the third point is proven.

A similar analysis may be performed to demonstrate that along the (A)–(C) boundary, there will be a point t_{AC} below which all trajectories intersecting the boundary will attempt to leave it. Those trajectories will slide up until they pass through t_{AC}. At that point, the trajectory slopes will then enter region (A). Together, the analyses indicate that trajectories starting outside of (A) will be reset to a saturation boundary on (A) and ultimately enter (A), demonstrating that the unsaturated region (A) is an attractive set for all trajectories starting outside of (A) (Fig. 19).

5.2. System behavior in the unsaturated region

Having established that the unsaturated region (A) is an attractive set for system trajectories, it is now necessary to show that all trajectories within (A) will converge to the equilibrium position. Once a system trajectory has entered (A), it will behave like one of the three trajectory types shown in Fig. 20. The trajectory will either

(1) asymptotically converge to the equilibrium position without further saturations;
(2) wrap around the equilibrium position and return to "impact" the saturation boundary that it originally came from; or
(3) the trajectory will cross (A), impact the opposite saturation boundary, return through (A), and impact the original saturation boundary.

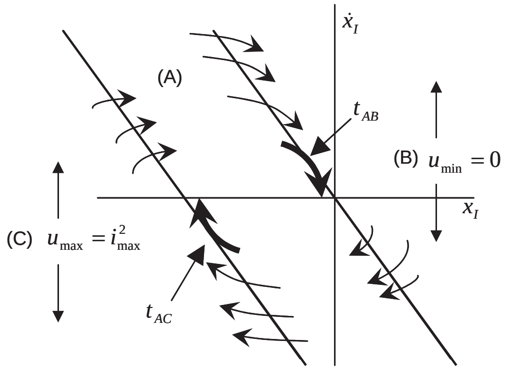

Fig. 19. Regions in the phase-plane and trajectory behavior along the saturation boundaries.

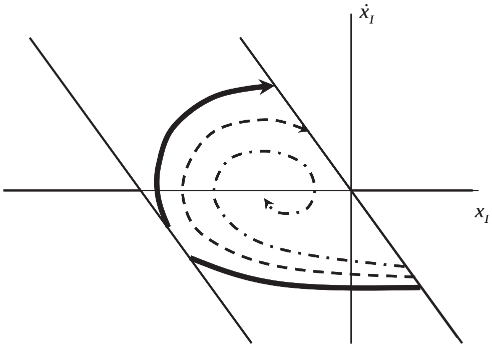

Fig. 20. Possible trajectory types: –·–, type (1); - - -, type (2); ——, type (3).

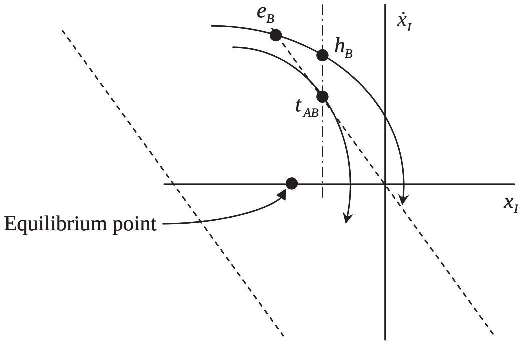

Fig. 21. t_B as the location of minimum $V(x_I, \dot{x}_I)$ along boundary (B)–(A).

The Lyapunov function, $V(x_I, \dot{x}_I)$, described by Eq. (6) is valid within and on the boundaries of the unsaturated region (A) in the $\{x_I, \dot{x}_I\}$ plane and can be used to show that system trajectories in groups (2) or (3) will eventually become trajectories in group (1). It is first important to note that along the (A)–(B) and (A)–(C) saturation boundaries, $V(x_I, \dot{x}_I)$ is at a minimum at t_{AB} and t_{AC}, respectively. This is demonstrated in Fig. 21. In the absence of saturation, a trajectory starting at a point along the (A)–(B) axis somewhere above t_{AB} will spiral out into region (B). The point where that trajectory leaves the (A)–(B) boundary is labeled e_B. When that trajectory attains the same x_I coordinate as t_{AB}, it will have a higher value of $\dot{x}_I$ as shown in Fig. 21. That point is labeled h_B. With identical x_I coordinates, $V(h_B) > (t_{AB})$ due to the second term in Eq. (6). Similarly, it can be shown that for trajectories along the (A)–(B) boundary below t_{AB}, $V(x_I, \dot{x}_I)$ will be larger than $V(t_{AB})$. As such, t_{AB} is the location of the minimal $V(x_I, \dot{x}_I)$ along the (A)–(B) saturation boundary. A similar analysis is used to show that $V(x_I, \dot{x}_I)$ is at a minimum at t_{AC} for trajectories along the (A)–(C) boundary.

Using these properties, if a trajectory "slides" down the (A)–(B) saturation boundary until t_{AB}, it can never return to the (A)–(B) saturation boundary. This is because $V(x_I, \dot{x}_I)$ will decrease in the unsaturated region, where $\dot{V}(x_I, \dot{x}_I) < 0$. If the trajectory does not impact the (A)–(C) boundary, then $V(x_I, \dot{x}_I)$ will continue to decrease and the trajectory will spiral in to the equilibrium position without further saturation. If the trajectory does, in fact impact the (A)–(C) boundary, then the implication is that $V(t_{AC}) < V(t_{AB})$. After sliding along (A)–(C) up until t_{AC}, the trajectory will then return to the unsaturated region, but can never return to the (A)–(B) boundary, as $V(x_I, \dot{x}_I)$ will have been decreasing both during the transit through region (A), as well as during the slide up to t_{AC}. From this analysis, it is proven that all trajectories eventually become type (1) trajectories and will converge to the solution $\cos(\phi_{\text{rel}}) = 0$.

To verify the analysis, the new nonlinear controller was implemented with the experimental setup described previously in Section 3. For this set of tests, the proportional gain was increased to $K_P = 88$, while the integral gain remained at $K_I = 26$. The purpose of doubling K_P was to test the anti-windup algorithm in a situation where overshoot and integrator windup would be severe. As for the earlier tests, the initial excitation was at 41 Hz, with subsequent steps up to 42.5 and 44 Hz, followed by steps down to 42.5 and 41 Hz. The time responses of the system to the initial 41 Hz excitation are shown in Fig. 22 for the controller with and without the anti-windup algorithm incorporated. The corresponding phase portraits are shown in Fig. 23.

The effect of the anti-windup algorithm is shown in the plots of $\cos(\phi_{\text{rel}})$ in Fig. 22. For both cases (with and without the anti-windup algorithm), there is an initial overshoot after the controller is turned on 30 s into the test. When the anti-windup algorithm was not included, further undershoot and overshoot events occur. By contrast, for the system with the anti-windup algorithm implemented, after the first overshoot, the system converges to the final answer without further oscillation. The reason for this behavior is shown in the plot of the current. After the initial overshoot, cooling is required to soften the SMA spring elements. Both systems saturate at $0\,\text{A}^2$. The standard linear controller experiences integrator windup, as shown by the longer period of zero power. The windup is reduced only after the controller integrates sufficient negative error. The system with the anti-windup algorithm included does not experience windup and thus converges to the steady state point relatively quickly. The anti-windup action is shown in the phase portrait of Fig. 23. It is apparent in that figure that the system experiences a type (3) trajectory as described above, where the system first saturates at the upper limit of the control effort, then passes through to saturate at the zero control effort saturation boundary.

While the plots of $\cos(\phi_{\text{rel}})$, the current, and the phase portraits illustrate the behavior of the controller, the most important element to be considered is the improved performance of the system when the anti-windup algorithm is used. In Fig. 22, the primary mass vibration decreases as both controllers drive the system to $\cos(\phi_{\text{rel}}) = 0$. After that first reduction however, the primary system vibration starts to increase due to the overshoot in $\cos(\phi_{\text{rel}})$. For the system with the standard linear controller, the amplitude of the vibration actually more than doubles before the integrator windup is reduced and the controller changes the tuning direction. For the case of the system with the anti-windup algorithm included, the performance is substantially improved. The initial overshoot is not as large as for the standard linear system and the control action brings the system to steady state much more quickly.

The improved performance of the system with the anti-windup algorithm is also shown in Figs. 24 and 25 where the system responses and phase portraits are shown for the step down in frequency from 42.5 to 41 Hz at 700 s into the test. For both systems, the initial vibration amplitude is very large. When the SMA ATVA is tuned to attenuate vibration at 42.5 Hz, a secondary resonance for the primary system is located at approximately 41 Hz. The sudden step down in frequency causes the primary system to be excited at that secondary resonance for a brief period of

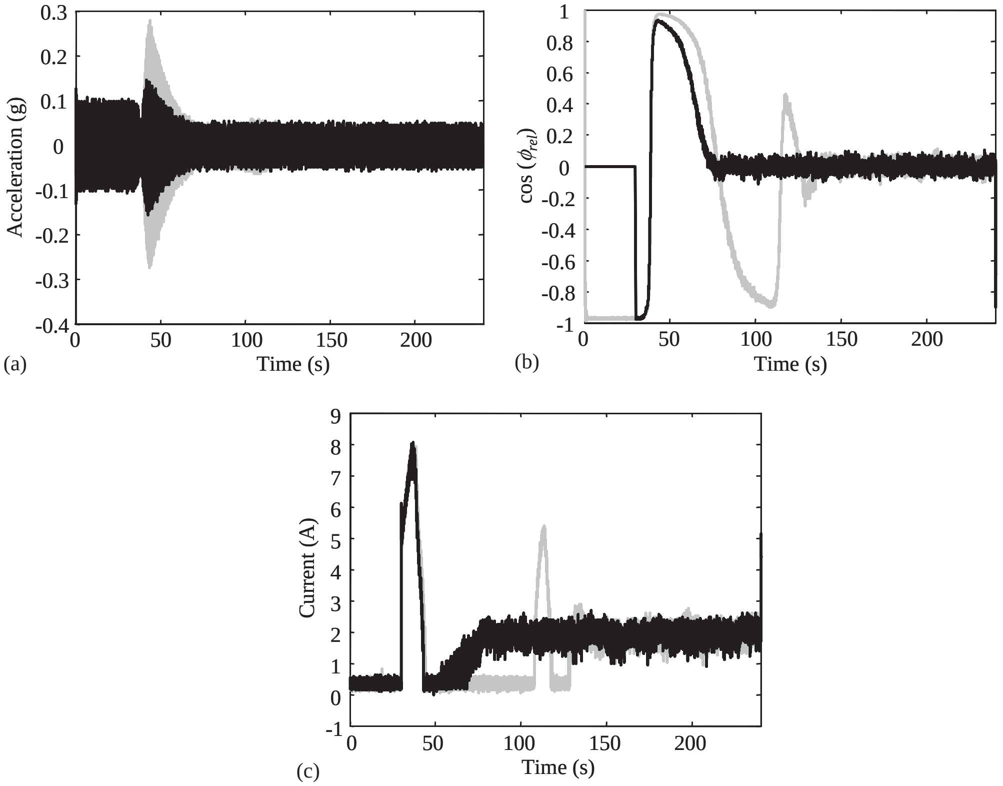

Fig. 22. SMA ATVA system response to 41 Hz excitation, $K_P = 88$, $K_I = 26$; □, without anti-windup; ■, with anti-windup. (a) Primary mass acceleration, (b) cosine of relative phase, (c) control current.

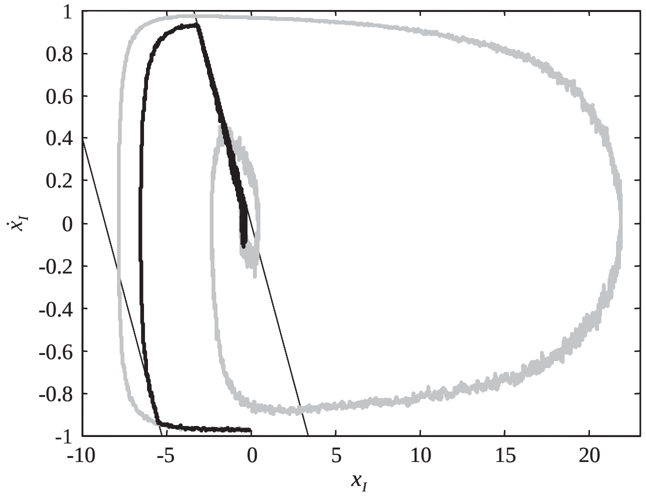

Fig. 23. SMA ATVA system phase portrait for system response to 41 Hz excitation, $K_P = 44$, $K_I = 26$: □, without; ■, with anti-windup.

time while the two controllers attempt to tune the SMA ATVA for the new excitation. In both cases, the controllers saturate at a squared current of 0 A^2. The trajectory for the system with the anti-windup algorithm implemented simply slides down the $u_{\min} = 0$ saturation boundary and converges to the steady-state solution without further saturation, as shown in Fig. 25. For the standard linear controller however, the integrator winds up and additional time passes before the system converges to steady state. The effect of the windup on the system performance is shown in the plot of the primary mass vibration shown in Fig. 24 where, after the initial reduction in vibration, the primary system vibration increases again as the system undershoots the final value of $\cos(\phi_{\mathrm{rel}})$.

In addition to demonstrating the performance improvements that are possible through the use of the anti-windup algorithm in the SMA ATVA controller, the more important result is that the system analysis has been validated. As expected, based on the Lyapunov analysis, the reset action guarantees operation within the unsaturated region of the phase plane and corresponding stability of the system.

One issue that has not been addressed is the overall system bandwidth. Control of the SMA ATVA is realized through variation of the SMA element temperature and is thus limited by the bandwidth of the temperature dynamics. During heating of the system, this may not be a significant issue. This is because implementation of the nonlinear controller permits the use of high gains, such that very large currents may be used to raise the SMA element temperature very

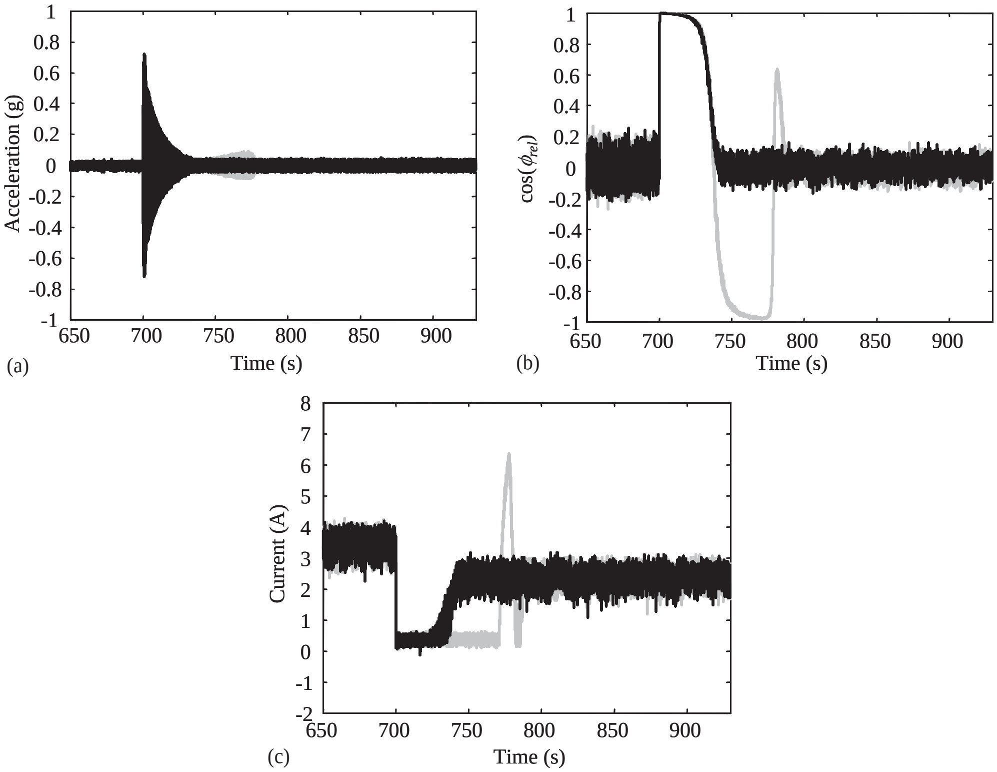

Fig. 24. SMA ATVA system response to step from 42.5 Hz down to 41 Hz excitation, $K_P = 88$, $K_I = 26$: ▢, without anti-windup; ■, with anti-windup. (a) Primary mass acceleration, (b) cosine of relative phase, (c) control current.

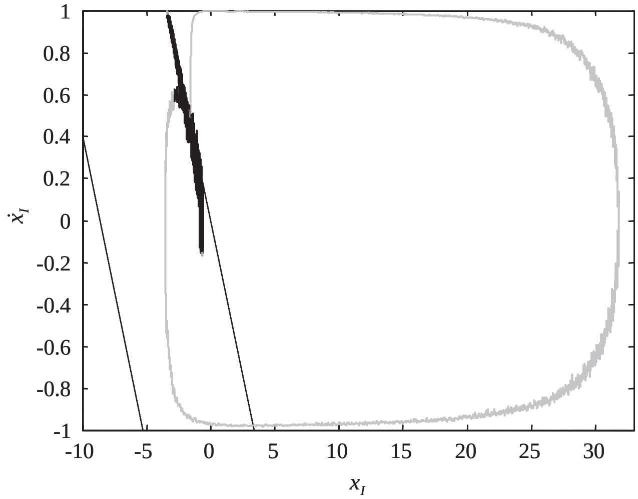

Fig. 25. SMA ATVA system phase portrait for system response to step from 42.5 Hz down to 41 Hz excitation, $K_P = 44$, $K_I = 26$: □, without; ■, with anti-windup.

quickly. During cooling, however, the rate of transformation is entirely dependent on the rate of heat removal from the SMA elements due to free convection. As such, the bandwidth of the system may be anticipated to be much slower for cooling, on the order of multiple seconds. Active cooling may be one method for addressing that issue and is the subject of future work in this area.

6. Conclusions

The development and experimental implementation of a nonlinear controller for an SMA ATVA was described in this work. The ATVA tuning problem was framed as a classical feedback control problem and a linear controller was developed. A Lyapunov analysis was presented to show that the resulting system was stable if controller saturation could be neglected. Due to the thermal actuation of the SMA tuning elements, controller saturation is expected, particularly especially when active cooling is not available. To deal with saturation, a nonlinear controller incorporating an anti-windup algorithm was developed. As shown in the experimental results, the modified controller works well and can substantially improve the performance of the system by avoiding integrator windup. In fact, while the controller was developed and successfully implemented with the SMA ATVA system, the controller has the potential to address the issue of integrator windup in similar nonlinear control problems. Future work will be directed to that end.

References

[1] J.Q. Sun, M.R. Jolly, M.A. Norris, Passive, adaptive, and active tuned vibration absorbers—a survey, *Journal of Mechanical Design* 117B (1995) 234–242.

[2] K.A. Williams, G.T.-C. Chiu, R.J. Bernhard, Dynamic modelling of a shape memory alloy adaptive tuned vibration observer, *Journal of Sound and Vibration* 280 (1 + 2) (2005) 211–234.

[3] K. Seto, N. Tominari, Effect of a variable stiffness-type dynamic damper on machine tools with long overhung ram, *Bulletin of the JSME* 19 (137) (1976) 1270–1277.

[4] M.A. Franchek, M.W. Ryan, R.J. Bernhard, Adaptive passive vibration control, *Journal of Sound and Vibration* 189 (5) (1995) 565–585.

[5] P.L. Walsh, J.S. Lamancusa, A variable stiffness vibration absorber for minimization of transient vibrations, *Journal of Sound and Vibration* 158 (2) (1992) 195–211.

[6] J.J. Hollkamp, T.F. Starchville, A self-tuning piezoelectric vibration absorber, *Journal of Intelligent Material Systems and Structures* 5 (4) (1994) 559–566.

[7] C.L. Davis, G.A. Lesieutre, An actively tuned solid-state vibration absorber using capacitive shunting of piezoelectric stiffness, *Journal of Sound and Vibration* 232 (3) (2000) 601–617.

[8] A.B. Flatau, M.J. Dapino, F.T. Calkins, High bandwidth tenability in a smart vibration absorber, *Proceedings of SPIE* 3327 (1998) 463–473.

[9] K.A. Williams, G.T.-C. Chiu, R.J. Bernhard, Passive-adaptive vibration absorbers using shape memory alloys, *Proceedings of SPIE* 3668 (1999) 630–641.

[10] C. Buhr, M.A. Franchek, R.J. Bernhard, Non-collocated adaptive-passive vibration control, *Journal of Sound and Vibration* 206 (3) (1997) 371–398.